

Classification and emergence of quantum spin liquids in chiral Rydberg models

Poetri Sonya Tarabunga ^{1,2,3}, Giuliano Giudici,^{4,5,6} Titas Chanda ¹ and Marcello Dalmonte ^{1,2}

¹*The Abdus Salam International Centre for Theoretical Physics (ICTP), Strada Costiera 11, 34151 Trieste, Italy*

²*International School for Advanced Studies (SISSA), via Bonomea 265, 34136 Trieste, Italy*

³*INFN, Sezione di Trieste, Via Valerio 2, 34127 Trieste, Italy*

⁴*Department of Physics and Arnold Sommerfeld Center for Theoretical Physics (ASC),*

Ludwig-Maximilians-Universität München, Theresienstraße 37, D-80333 München, Germany

⁵*Munich Center for Quantum Science and Technology (MCQST), Schellingstraße 4, D-80799 München, Germany*

⁶*Institute for Theoretical Physics, University of Innsbruck, A-6020 Innsbruck, Austria*



(Received 29 March 2023; revised 26 July 2023; accepted 28 July 2023; published 7 August 2023; corrected 24 January 2024)

We investigate the nature of quantum phases arising in chiral interacting Hamiltonians recently realized in Rydberg atom arrays. We classify all possible fermionic chiral spin liquids with $U(1)$ global symmetry using parton construction on the honeycomb lattice. The resulting classification includes six distinct classes of gapped quantum spin liquids: the corresponding variational wavefunctions obtained from two of these classes accurately describe the Rydberg many-body ground state at $1/2$ and $1/4$ particle density. Complementing this analysis with tensor network simulations, we conclude that both particle filling sectors host a spin liquid with the same topological order of a $\nu = 1/2$ fractional quantum Hall effect. At density $1/2$, our results clarify the phase diagram of the model, while at density $1/4$, they provide an explicit construction of the ground-state wavefunction with almost unit overlap with the microscopic one. These findings pave the way to the use of parton wavefunctions to guide the discovery of quantum spin liquids in chiral Rydberg models.

DOI: [10.1103/PhysRevB.108.075118](https://doi.org/10.1103/PhysRevB.108.075118)

I. INTRODUCTION

There is presently considerable interest in studying strongly correlated phases of matter in synthetic quantum systems based on Rydberg atom arrays [1,2]. Stimulated by early experiments realizing symmetry-protected topological phases in one dimension [3], these platforms are now able to realize frustrated Hamiltonian dynamics in two dimensions [4–6], thus providing unparalleled opportunities to realize quantum spin liquids (QSLs)—elusive, exotic states of matter, which have captivated the attention of physicists for decades [7–10]. One route to access QSLs is based on the realization of frustrated Ising models in the so-called frozen gas regime [2,11,12]: Several theoretical works have proposed different realistic scenarios for both gapped and gapless phases of matter [13–16], with pioneering experiments already reporting evidence for deconfinement [6]. These models resemble closely situations investigated in the context of quantum dimer models [17], providing direct link between gauge theories and experimental settings [18–21].

Over the last two years, a new route has been paved in a very different experimental regime, where the dynamics solely takes place within the Rydberg subspace. The resulting Hamiltonians naturally feature various forms of chiral multibody interactions [22–25], which have already been experimentally demonstrated [26]. These classes of dynamics differ fundamentally from traditional Ising- and Heisenberg-type frustrated magnets and, while very promising since they display chiral terms, it is presently not even clear what classes of quantum spin liquids these can stabilize, and in which parameter regimes they might be observed.

In this paper, we provide a general framework to describe chiral spin liquids (CSLs) in Rydberg atom honeycomb arrays. This framework is based on a systematic CSLs classification [27–29] using a fermionic spinon construction [30,31] that yields Gutzwiller-projected parton wavefunction *ansätze* for the many-body ground state. The resulting classification differs substantially from those of Heisenberg-type regimes: it rules out the possibility of gapless Dirac spectrum, while predicting several, distinct topological phases.

Combining variational wavefunctions obtained from the classification with exact diagonalization (ED) methods, we demonstrate that the former capture the intermediate liquid regime of the chiral Rydberg model at both $1/2$ [25] and $1/4$ density [24], which—surprisingly—encode the same form of topological order: a twofold ground-state degeneracy and a fractionalized Chern number $C = 1/2$ per state. These two CSLs represent two distinct phases characterized by different projective representations of the lattice symmetries in the underlying fermionic spinon space. Remarkably, the CSL at $1/2$ density is a new phase, which corresponds to integer filling of the single-particle band, thereby representing an interaction-driven topological phase generated from a trivial band insulator [32], setting an open quest recently put forward in Ref. [25]. We then corroborate the topological character of this phase by computing the topological correction to the area-law scaling of entanglement entropy [33,34], which is consistent with a CSL ground state, and by analyzing the pattern of currents at the edges of a cylinder using the density matrix renormalization group (DMRG) [35–38], which shows substantial counter-propagating nearest-neighbor edge currents,

offering a simple mean for experimental detection. In the 1/4-density case, our results allow to frame the recent observation of CSL [24] within a rigorous classification, as well as providing a genuine understanding of the system wavefunction.

The rest of the paper is structured as follows. In Sec. II, we introduce the model under study and give a brief overview of previous studies on its phase diagram. In Sec. III, we present the classification of CSL on the honeycomb lattice with appropriate symmetries of the Rydberg model. The microscopic wavefunctions resulting from the classification are then compared with the ground-state wavefunction of the model in Sec. IV. Here, we show that the overlaps are significant in the intermediate phase, strongly indicating that the phase is a CSL. In Secs. V, VI, and VII, we show additional numerical results on excitation spectra, topological entanglement entropy, and chiral edge currents, respectively, which further confirm the CSL nature of the intermediate phase. Then, in Sec. VIII, we discuss a putative intermediate phase intervening between the CSL and the BEC phase. Finally we conclude in Sec. IX.

II. MODEL HAMILTONIAN AND PHASE DIAGRAM

We consider a system with atoms arranged on a honeycomb lattice. We assume optical control on the three Rydberg states $|0\rangle$, $|+\rangle = a^\dagger|0\rangle$, and $|-\rangle = b^\dagger|0\rangle$, where the state $|0\rangle$ has no excitations, and the states $|+\rangle$ and $|-\rangle$ (which belong to the same Rydberg manifold and differ, e.g., by their total angular momentum) encode two species of hard-core bosons created by the operators a^\dagger and b^\dagger , respectively. Atomic motion is irrelevant on typical experimental timescales: below, we focus on the dynamics of the Rydberg excitations. The model Hamiltonian is [22,23]

$$H_0 = \sum_{i \neq j} \begin{pmatrix} a_i \\ b_i \end{pmatrix}^\dagger \begin{pmatrix} -t_{ij}^a & w_{ij}e^{-i2\phi_{ij}} \\ w_{ij}e^{i2\phi_{ij}} & -t_{ij}^b \end{pmatrix} \begin{pmatrix} a_j \\ b_j \end{pmatrix} + \frac{\mu}{2} \sum_i (n_i^a - n_i^b). \quad (1)$$

The first term represents hopping processes (of excitations) between different sites, with the real hopping conserving the internal state, and the complex hopping resulting in a change of the internal state. The amplitudes for real and complex hoppings are given by t_{ij}^a , t_{ij}^b , and $w_{ij}e^{\pm i2\phi_{ij}}$ respectively, with ϕ_{ij} being the polar angle between the two Rydberg atoms on the sites i and j . All the amplitudes scale as $1/r_{ij}^3$. The second term represents the energy difference between the two internal states, with n_i^a and n_i^b being the particle number operators for the $|+\rangle$ and $|-\rangle$ states, respectively.

Here, we focus on the regime $\mu \gg t_{ij}^a, t_{ij}^b, w$, in which case the internal state $|+\rangle$ can be adiabatically eliminated. We further make an approximation by considering only nearest-neighbor (NN) interactions in Eq. (1), with NN hopping amplitudes t^a , t^b , and $w e^{\pm i2\phi_{ij}}$. A more detailed discussion of the validity of this approximation can be found in Appendix A. At leading order, the effective Hamiltonian is given by [26]

$$H = -J \sum_{\langle ij \rangle} b_j^\dagger b_i - 2gJ \sum_{\langle\langle ij \rangle\rangle} b_j^\dagger b_i e^{\pm 2\pi i/3} (1 - n_{ij}) + \text{H.c.} + 4gJ \sum_{\langle ij \rangle} n_i n_j, \quad (2)$$

where $J = t^b$ and $g = w^2/(2\mu)$. The complex phases $e^{\pm 2\pi i/3}$ in the next-nearest-neighbor (NNN) hopping are illustrated in Fig. 1(a). The NNN hoppings explicitly break time-reversal and reflection symmetries, but preserves their combination. The Hamiltonian has U(1) symmetry related to particle-number conservation. Note that, in the language of spins, the U(1) symmetry corresponds to spin-rotation symmetry around the z axis. Hereafter, we set the energy scale to $J = 1$.

The phase diagram of the model at 1/2 density has been studied in Ref. [25], where three different phases were found for $g \geq 0$. For $g \lesssim 0.4$, the phase is a Bose-Einstein condensate (BEC), while for $g \gtrsim 0.9$ the phase exhibits spiral or 120° spin order [39]. The intermediate phase between $0.4 \lesssim g \lesssim 0.9$, shows no clear order, and it is believed to be a candidate for a spin liquid. However, its true nature remains unclear, also due to hard-to-interpret spectral properties.

At 1/4 density, Ref. [24] investigated the full model in Eq. (1) and provided clear numerical evidence for a fractional Chern insulating state: that included ground-state degeneracy and Chern number compatible with a $\nu = 1/2$ bosonic Fractional Quantum Hall (FQH) state. Building on such numerical understanding, we will show below how that reflects into a very clear ansatz for the system wavefunction, informed by our classification.

III. CLASSIFICATION AND VARIATIONAL WAVEFUNCTIONS FROM PARTON CONSTRUCTION

In order to construct a spin liquid wavefunction, a method based on fermionic representation of spins have been introduced in [30,31]. The main idea is to fractionalize the spin-1/2 operators into fermionic spinon operators as $S^a = \frac{1}{2} f_i^\dagger \sigma_i^a f_j$, where σ^a are Pauli matrices, with the constraint of one spinon per site. It is convenient to introduce a two-component spinor $\Psi = (f_\uparrow, f_\downarrow)^T$. Directly rewriting the spins in terms of spinons gives rise to quartic spinon interactions, which after performing mean-field approximation, leads to a quadratic spinon Hamiltonian

$$H_{MF} = \sum_{ij} \Psi_i^\dagger u_{ij} \Psi_j + \text{H.c.}, \quad (3)$$

where u_{ij} are the mean-field amplitudes. The spinon interactions include hopping and pairing terms. The mean-field Hamiltonian is invariant under global spin rotation around the z axis [40,41]. The matrices u_{ij} can be written as $u_{ij} = u_{ij}^\mu \sigma^\mu$, where $(\sigma^\mu) = (i\tau^0, \tau^a)$, u_{ij}^μ are complex parameters and τ^a are Pauli matrices. Real u_{ij}^μ correspond to singlet terms, while imaginary u_{ij}^μ correspond to triplet terms [42]. Different mean-field ansätze are described by different (gauge-inequivalent) $\{u_{ij}\}$ on the links of the lattice. Finally, a physical spin state is obtained by applying Gutzwiller projection $|\psi\rangle = P_G |\psi_{MF}\rangle$, with $P_G = \prod_i n_i(2 - n_i)$, to the mean-field ground state $|\psi_{MF}\rangle$.

A method to systematically classify all possible spin liquids within this parton construction has been introduced by Wen [27,28,43], based on projective symmetry groups (PSG). It has subsequently been extended to classify spin liquid phases in the absence of time-reversal (i.e., CSL) [29] and SU(2) spin-rotation [40,41] symmetries. Here, we are

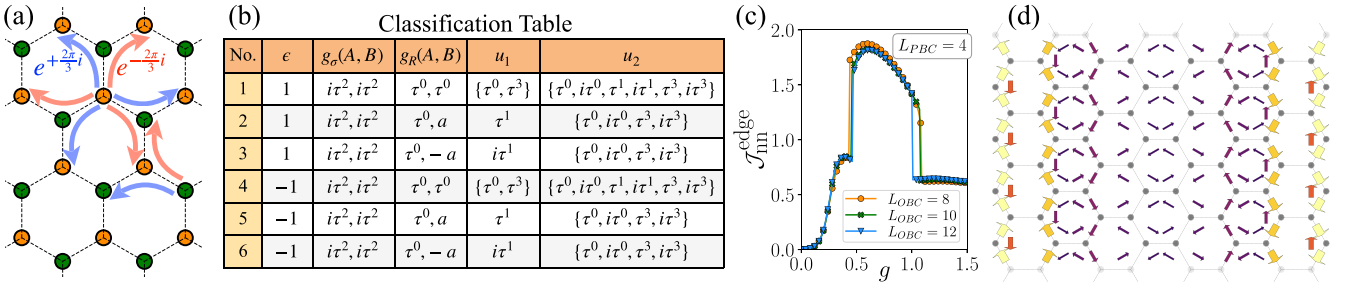


FIG. 1. (a) Schematics of the model on the honeycomb lattice. The signs of the complex phase in the next-nearest-neighbor (NNN) hoppings are indicated by the colored arrows. (b) Mean-field ansätze of chiral spin liquids on the honeycomb lattice with broken time-reversal and reflection symmetries. ϵ indicates whether the unit cell is doubled in the spinon space. $g_\sigma(A/B)$ and $g_R(A/B)$ are projective representations of reflection and rotation symmetries, respectively, with $a = e^{i2\pi/3\tau^3}$. u_1 and u_2 are mean-field amplitudes at NN and NNN links, respectively. The CSL phase at 1/2 and 1/4-density are captured by ansatz no. 1 and 4, respectively. (c) NN edge currents for cylinders with periodic width $L_{\text{PBC}} = 4$ (i.e., eight lattice sites). The edge currents are substantially larger in the intermediate phase compared to the neighboring phases. (d) The current profile at $g = 0.74$ for a cylinder with periodic width $L_{\text{PBC}} = 4$ and length $L_{\text{OBC}} = 8$. Widths of the arrows are proportional to the current values and directions denote the current directions. Large counterpropagating NN currents are observed only at the edges, while they vanish in the bulk.

interested in a CSL, which breaks time-reversal and reflection symmetries but preserve their combination, and which preserves $U(1)$ spin-rotation symmetry. Such chiral mean-field states are stable beyond mean-field treatment, as the mean-field gauge fluctuations are gapped out by the Chern-Simons mechanism [44].

The PSG classification of symmetric spin liquids on the honeycomb lattice has been worked out in [45], where 160 different algebraic PSG's are found. In the absence of time-reversal symmetry, we do not need to specify the $SU(2)$ representation of the time-reversal operation [29]. Thus, we find that the number of different classes of algebraic PSG is reduced to 24 (see Appendix B). Each PSG is characterized by the representations of reflection $g_\sigma(A, B)$, and $\pi/3$ rotation $g_R(A, B)$, for each sublattice A and B (for more technical details, see Appendix B).

Given the model that we study, we focus on those ansätze that have nonzero mean-field amplitudes on the NN and NNN links. This leaves six distinct ansätze, which are listed in the Fig. 1(b). The last two columns indicate the symmetry-allowed terms in the mean-field Hamiltonian on the NN and NNN links [46]. Their amplitudes are taken as variational parameters in the following section.

Note that if the ansätze are restricted to NN interactions, the mean-field states are gapless with Dirac spectrum (in particular, ansatz no. 1 corresponds to the $SU(2)$ algebraic spin liquid (ASL) state discussed in [47], or equivalently the u-RVB state discussed in [45]). Thus, the resulting states after Gutzwiller projection describe a Dirac spin liquid (DSL). However, this DSL ansatz submanifold preserves time reversal, which is explicitly broken by our Hamiltonian. This excludes the possibility of a DSL being stabilized in chiral systems such as our model.

IV. OVERLAPS WITH GUTZWILLER-PROJECTED PARTON WAVEFUNCTIONS

To determine whether the intermediate phase of the model in Eq. (2) is described by one of the ansätze above, we optimize the variational parameters by maximizing the overlap

of the exact ground state of the Hamiltonian with the wavefunction ansatz, for each of the six ansätze. The optimization of the overlap is performed using the Nelder-Mead optimization method, implemented in MATLAB. The optimization is performed on a 16-site cluster at $g = 0.7$. We find that the ansatz with the largest overlap with the ground state at 1/2 density is ansatz no. 1, characterized by nonzero real triplet NN hopping parameter τ^0 , imaginary singlet NNN hopping parameter $i\tau^0$, and imaginary triplet NNN hopping parameter $i\tau^3$. The corresponding amplitudes are $u_2^{i\tau^0}/u_1^{\tau^0} = -0.31$ and $u_2^{i\tau^3}/u_1^{\tau^0} = -0.1$. We have also checked that the optimal parameters do not differ much from the optimal parameters on the smaller clusters.

The spinon band structure with the optimal parameters are shown in Fig. 3(a). Note that each band is spin degenerate. With one fermion per site, the mean-field ground state is obtained by filling all single-particle orbitals in the lower band, for both spin-up and spin-down orbitals. There is a finite-energy gap to the valence band, resulting in a fully gapped state. The Gutzwiller projection of such an ansatz has been shown to yield a topological CSL [44,48,49], which is a lattice analog of $\nu = 1/2$ FQH Laughlin state [50]. The topological nature of such CSL is manifested by the twofold topological degeneracy of states on a torus. These degenerate states can be constructed by threading fluxes along the non-contractible loops on a torus [51], which can be implemented

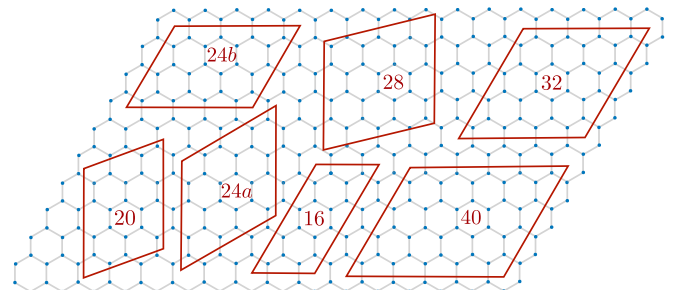


FIG. 2. Periodic clusters used for the exact diagonalization calculations.

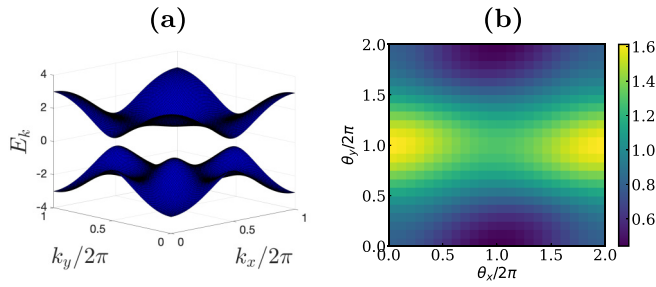


FIG. 3. (a) Spinon band structure and (b) Berry curvature on the cluster 24b (normalized with the average) of the optimal ansatz at $g = 0.7$ for $n = 1/2$. The parameters are $u_2^{i\tau^0}/u_1^0 = -0.31$ and $u_2^{i\tau^3}/u_1^0 = -0.1$.

by twisting the boundary conditions of the spinons, $\Psi \rightarrow e^{i\theta/2}\Psi$. Although there are four states that can be constructed with $\theta_x, \theta_y \in \{0, \pi\}$, they only span a two-dimensional space, resulting in two topological states. We verify this numerically by computing the overlap matrix for the four states, defined as $O_{ij} = \langle \psi_j | \psi_i \rangle$. We find that the rank of the overlap matrix is 2, within a numerical accuracy on the order of 10^{-2} . The two independent states are then constructed from the eigenvectors of the overlap matrix with nonzero eigenvalues.

Furthermore, we computed the many-body Chern number, a topological invariant that characterizes the topologically nontrivial phases of matter [52]. It can be computed by twisting the boundary condition by angles $\theta_{x,y}$ in the x, y direction, and is given by the integral of the Berry curvature over the twist space,

$$C = \frac{1}{2\pi i} \int_0^{2\pi} \int_0^{2\pi} d\theta_x d\theta_y \left(\langle \partial_{\theta_x} \Psi(\theta) | \partial_{\theta_y} \Psi(\theta) \rangle - \langle \partial_{\theta_y} \Psi(\theta) | \partial_{\theta_x} \Psi(\theta) \rangle \right), \quad (4)$$

where $|\Psi(\theta)\rangle = |\Psi(\theta_x, \theta_y)\rangle$ is the ground-state wavefunction with twist angles θ_x and θ_y . To compute Eq. (4) numerically, we discretize the twist space into $D \times D$ mesh and sum the discretized Berry curvature. We have obtained $C = 2$, with the Berry curvature for $D = 24$ is shown in Fig. 3(b). Note that the twist $0 \leq \theta_{x,y} \leq 2\pi$ for the fermionic spinon operators corresponds to 0 to 4π twist for the spin operators, and therefore, the result must be divided by 4. Thus, the Chern number of the spin wavefunction is fractionalized $C = 1/2$ per state. The Chern number, along with the twofold degeneracy, are consistent with the properties of $\nu = 1/2$ bosonic Laughlin state.

Having established the FQH nature of the ansatz, we next compute the overlap of the ground state of the Hamiltonian with the two topological states [53,54],

$$\mathcal{O}_{GW}^{ED} = \sqrt{|\langle \psi_{ED} | \psi_{GW}^1 \rangle|^2 + |\langle \psi_{ED} | \psi_{GW}^2 \rangle|^2}, \quad (5)$$

where $|\psi_{ED}\rangle$ is the ground state obtained with ED and $|\psi_{GW}^1\rangle$ and $|\psi_{GW}^2\rangle$ are the two topological states. All the ED clusters that are considered are depicted in Fig. 2. We impose periodic boundary conditions, and the ED calculations are performed exploiting translational symmetry. The cluster 24a and the 32-site cluster has sixfold rotational symmetry, which we also exploit.

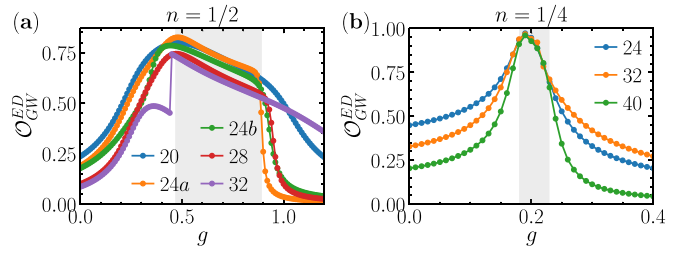


FIG. 4. Overlaps \mathcal{O}_{GW}^{ED} between the exact ground states with (a) ansatz no. 1 at $1/2$ density and (b) ansatz no. 4 at $1/4$ density. The shaded region denotes the intermediate phase, which we show to be a CSL.

The results are shown in Fig. 4(a) for different system sizes. It can be seen that the overlap remains large in the middle phase with increasing system size, indicating that the ground state is strongly related to the topological states. Interestingly, on a 32-site cluster, we find that the ground state in the intermediate phase is not in the rotation-neutral sector. Specifically, if we take the operator $R_{\pi/3}$, which generates a $\pi/3$ rotation around the center of a honeycomb plaquette, then $R_{\pi/3}|\psi_{ED}\rangle = e^{-2\pi i/3}|\psi_{ED}\rangle$. This can be seen in Fig. 4(a) as a discontinuous jump in the overlap at $g \approx 0.45$, as the transition from the BEC phase becomes a level crossing between different rotation sectors. Remarkably, one of the two topological states is in the same nontrivial rotation sector as the ground state of the Hamiltonian, i.e., the eigenvalue of $R_{\pi/3}$ is $e^{-2\pi i/3}$. This nontrivial observation strongly supports the hypothesis that the intermediate phase is described by the wavefunction ansatz.

At this point, it is worth emphasizing that the CSL phase found at $1/2$ density represents a novel phase that has not been previously identified. Notably, this CSL has a dispersive band [see Fig. 3(a)], distinguishing it from the previously observed CSLs at $1/4$ density [24,55] and $1/8$ density [55] that possesses topological flat bands. As such, this CSL is inevitably missed by previous approaches relying on the identification of flat bands [24,55]. Moreover, its dispersive band significantly affects the physical properties on finite-size clusters, thus hindering the identification of the true CSL nature in previous study [25]. Our hybrid approach, combining theoretical PSG classification and numerical optimization, thus showcases its effectiveness by successfully identifying the CSL phase even in the presence of strong finite-size effects.

To compare with the $1/2$ -density case, we performed the same parameter optimization procedure for the $1/4$ -density case. In [24], it was shown that a CSL emerges at $1/4$ density for the full model in Eq. (1). For the effective model in Eq. (2), we found that the CSL phase emerges in a narrow range around $g = 0.2$. For $1/4$ density, a gapped phase can be obtained within the parton construction when the mean-field ansatz has a doubled unit cell. We obtain large overlaps with the ansatz no. 4 at small-size clusters in the CSL phase. Figure 4(b) shows the overlaps for $1/4$ density with the optimized parameter for different system sizes. We found that the overlap remains huge in the CSL phase, reaching 0.96 at the largest system size we considered, $L = 40$.

In Fig. 5, we present the excitation spectrum in the momentum sector $k = (0, 0)$ at $g = 0.1$ and $g = 0.7$, along with

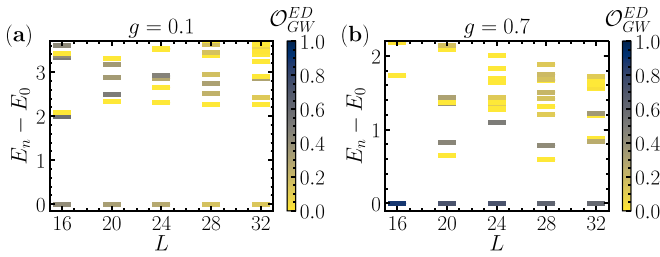


FIG. 5. Excitation spectrum in the momentum sector $k = (0, 0)$ up to the 10th excited state for (a) $g = 0.1$ and (b) $g = 0.7$ at $1/2$ density. The markers are colored according to the overlap \mathcal{O}_{GW}^{ED} .

the overlaps \mathcal{O}_{GW}^{ED} for each eigenstate. Note that, since the two topological states $|\psi_{GW}^1\rangle$ and $|\psi_{GW}^2\rangle$ lie in the momentum sector $k = (0, 0)$, only the eigenstates in this sector can have nonzero overlap. In agreement with [25], we observe no approximate twofold degeneracy in the ED spectra, which would have been expected in a CSL. Nevertheless, this can be attributed to finite-size effects, which may significantly modify the spectra on small-size clusters. It is therefore possible that one of the low-lying states corresponds to another topological ground state, which becomes degenerate with the true ground state in the thermodynamic limit. To test this hypothesis, it is useful to examine the overlaps of the low-lying levels. If an eigenstate describes the topological ground state of the CSL, it would have a sizable overlap with the wavefunction ansatz. Indeed, at $g = 0.7$, we observe that the overlap is highest for the ground state, and that there is a low-lying state with a modest overlap. In contrast, at $g = 0.1$, the overlaps do not exhibit any clear pattern for each system size.

V. EXCITATION SPECTRA

In Ref. [25], a DSL was proposed as one of possible scenarios, based on the observation that the gap to the first excited state varies significantly with twist angle when imposing twisted boundary conditions. In light of this, we analyze the excitation gaps as a function of twist angles $\theta_{1,2}$ along the lattice vectors $\vec{a}_{1,2}$. In Fig. 6(a), we show the gap to the first excited state obtained with ED on a 24-site cluster, while the gap to the second excited state and the (symmetrized) charge gap are shown in Figs. 6(b) and 6(c), respectively. We observe that while the first gap may become very small at some isolated points in twist space, the second gap and charge gap remain wide open. This contrasts with the expected behavior of a DSL, where all gaps would exhibit a vanishing behavior with respect to twist angles [56–58]. In addition, the transfer matrix spectrum does not show any signatures of Dirac cones (see Appendix E). This is consistent with our results that DSL is unstable against time-reversal symmetry breaking perturbations (see Sec. III).

We note that the drastic variation of the first gap with respect to the twist angles becomes even more pronounced at larger sizes, as can be seen in the cluster of $L = 32$ sites shown in Fig. 6(d). Based on our findings, we are able to offer an interpretation of the curious vanishing of the gap to the first excited state as observed in [25]. Indeed, for a CSL two topological ground states will flow into each other upon inserting

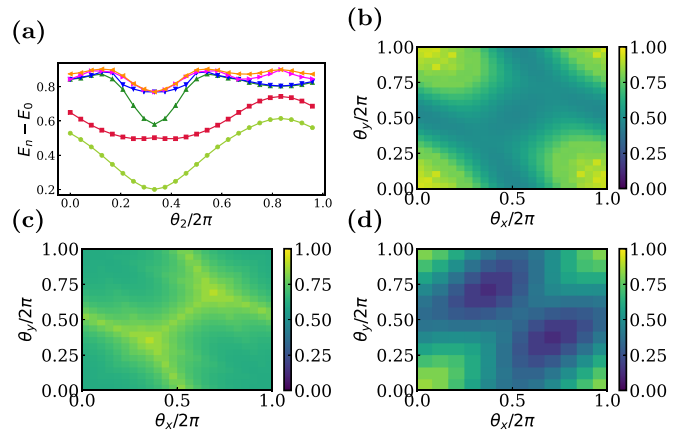


FIG. 6. (a) Excitation spectrum on the cluster 24a at $g = 0.7$ with twist $\theta_1 = 2\pi/3$ and varying θ_2 . (b) Gap to the second excited state $E_2 - E_0$, and (c) (symmetrized) charge gap $\Delta^c(N) = \frac{1}{2}(E(N+1) + E(N-1) - 2E(N))$ with $N = L/2$ as a function of the twist angles $\{\theta_1, \theta_2\}$ on the cluster 24a. (d) Gap to the first excited state $E_1 - E_0$ in the $k = (0, 0)$ momentum sector on the 32-site cluster as a function of the twist angles $\{\theta_1, \theta_2\}$.

flux (see, e.g., [55]). In the case of CSL at $n = 1/2$ density, the two ground states live in the same $k = (0, 0)$ momentum sector. Consequently, the flow between these ground states manifests as an avoided crossing. As a result, the gap appears to vanish at some isolated points, corresponding precisely to the locations where the avoided crossing occurs. This behavior is specific to the first gap and not observed in higher gaps or the charge gap, as the CSL is gapped to all excitations. This is consistent with our results on excitation spectra discussed above.

VI. TOPOLOGICAL ENTANGLEMENT ENTROPY

A topological phase can be characterized by the scaling of the entanglement entropy. The entanglement entropy for a region with perimeter L is known to scale as $S(L) = \alpha L - \gamma$, where the subleading term γ is a universal constant called the topological entanglement entropy, which characterizes the topological order in a ground-state wavefunction [33,34]. Here, we employ the Kitaev-Preskill scheme [33] to compute γ ,

$$\gamma = S_{AB} + S_{BC} + S_{AC} - S_A - S_B - S_C + S_{ABC}, \quad (6)$$

where the partitioning is depicted in Fig. 7(a). In Fig. 7(b), we show the behavior of γ in the exact ground state obtained with ED for $n = 1/2$ density. In the CSL phase, even in small systems, the computed γ is finite, and close to the expected value $\gamma = \frac{1}{2} \log(2)$ for a $\nu = 1/2$ FQH state [59].

VII. CHIRAL CURRENTS

Quantum Hall states can be identified through the pattern of the currents in the system. With a finite gap in the bulk and gapless edge excitations on the boundary, it is expected that the currents are large at the edges and vanish in the bulk. Furthermore, the current can be readily measured in experiments, making it a convenient tool for diagnosing the

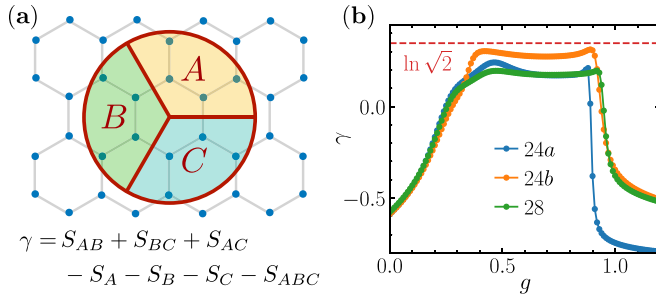


FIG. 7. (a) Partitions used for the topological entanglement entropy calculation. (b) Topological entanglement entropy γ as a function of g at $1/2$ density, obtained from the exact ground state on different periodic clusters (see Fig. 2). The dashed red line is the value of γ expected for a $\nu = 1/2$ FQH state.

phase in experimental setups. The NN and NNN currents can be derived using the continuity equation, resulting in

$$\begin{aligned} \mathcal{J}_{nn} &= i\langle b_j^\dagger b_i - b_j b_i^\dagger \rangle, \\ \mathcal{J}_{nnn} &= 2g e^{\pm 2\pi/3i} \langle (1 - n_{ij})(b_j^\dagger b_i - b_j b_i^\dagger) \rangle, \end{aligned} \quad (7)$$

where i and j are nearest-neighbors or next to nearest-neighbors respectively.

We perform DMRG simulations on a finite cylinder to compute the edge currents as a function of g , as shown in Fig. 1(c) [60]. It can be seen that the NN edge currents, computed across two rungs in one of the edges, in the intermediate phase are significantly larger compared to those in the neighboring phases. The transition points are in good agreement with those found in [25]. Furthermore, we show the full current profile in the intermediate phase ($g = 0.74$) in Fig. 1(d). It is clear that, in the CSL phase, large NN currents are only observed at the edges, while they vanish in the bulk. The full current profile is shown for each phases in Fig. 8. Clearly, substantial counter-propagating NN edge currents manifests only in the CSL phase that vanish in the bulk. On the other hand, most dominant currents in the other phases are of the NNN nature that originate from the NNN term in the Hamiltonian.

VIII. ANOTHER INTERMEDIATE PHASE

Notice that Fig. 1(c) also exhibits signatures of another intermediate phase with nonzero edge currents for $0.25 \lesssim g \lesssim 0.4$. While its full characterization is beyond the scope of this paper, we report here our preliminary findings on this possible new phase.

To detect transition points and obtain the phase diagram as a function of g , we compute the fidelity-susceptibility χ_F defined as

$$\chi_F(g) = \frac{2}{L} \lim_{\delta g \rightarrow 0} \frac{-\ln F(g, \delta g)}{(\delta g)^2} \quad (8)$$

where the fidelity F is defined as $F(g, \delta g) = |\langle \psi(g) | \psi(g + \delta g) \rangle|$. The fidelity susceptibility χ_F is known to be a good indicator for quantum phase transition, whose critical point can be derived via finite-size scaling techniques [61]. In case

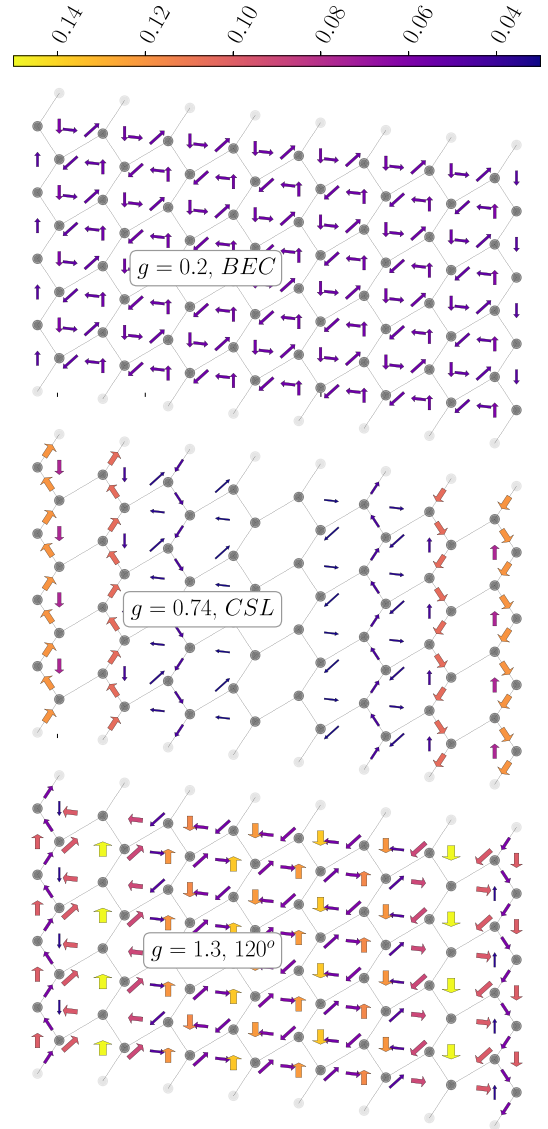


FIG. 8. Full current profiles at $n = 1/2$ filling for the cylinders with geometry I and with periodic width $L_{\text{PBC}} = 4$ and length $L_{\text{OBC}} = 8$ for three representative values of g inside three phases, namely BEC (top), CSL (middle), and the 120° (bottom) phases. The widths of the arrows are proportional to the magnitudes of the current, while their direction indicates the directions of respective currents.

of iDMRG simulations, however, we have

$$F(g, \delta g) = \lim_{L \rightarrow \infty} |\eta|^L, \quad (9)$$

where η is the dominant eigenvalue of the transfer matrix constructed from the iMPS ansatz of $|\psi(g)\rangle$ and $|\psi(g + \delta g)\rangle$. Since, for two normalized iMPS $|\psi(g)\rangle$ and $|\psi(g + \delta g)\rangle$, $|\eta| < 1$ for $\delta g \neq 0$, we get $F(g, \delta g) \rightarrow 0$ as $L \rightarrow \infty$. The fidelity susceptibility can be expressed as

$$\chi_F(g) = -2 \ln |\eta|, \quad (10)$$

which remains finite.

We show the fidelity susceptibility obtained using iDMRG for two different types of cylinders in Fig. 9(a). The emergence of the CSL phase can be identified in the parameter

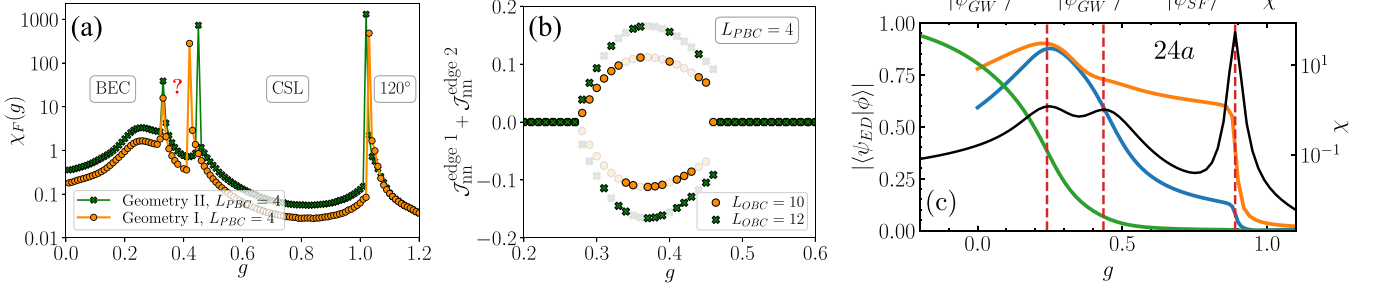


FIG. 9. (a) The fidelity susceptibility $\chi_F(g)$ as a function of g for infinite cylinders with two different geometries and with periodic width $L_{PBC} = 4$ in the $n = 1/2$ density regime. The $\chi_F(g)$ shows the existence of a new phase sandwiched between the BEC and the CSL phases. (b) The total nearest-neighbor edge current $\mathcal{J}_{nn}^{\text{edge } 1} + \mathcal{J}_{nn}^{\text{edge } 2}$ computed for finite cylinders of geometry I and with periodic width $L_{PBC} = 4$ for $n = 1/2$ density. In the new intermediate phase, reflection \times time-reversal symmetry gets spontaneously broken, and the total edge current becomes finite (positive or negative). Since, the DMRG simulations breaks this \mathbb{Z}_2 symmetry somewhat randomly, there is an arbitrariness in the sign of the edge current. That is why transparent symbols are added that represent the currents with opposite signs of the actual DMRG data. (c) Fidelity susceptibility and overlaps of the exact ground state with various ansatz on the cluster 24a for $n = 1/2$. Orange line: overlap with ansatz no. 1 optimized at each point. Blue line: Overlap with DSL wavefunction with uniform spin-dependent NN hopping τ^0 . Green line: Overlap with superfluid ansatz, defined as the equal-weight superposition of all states at fixed density. The emergence of the additional phase can already be observed, between the two nearby peaks of fidelity susceptibility at $g = 0.24$ and $g = 0.43$, which are denoted by the vertical red lines. The overlap with DSL wavefunction peaks close to the transition between the BEC phase and the additional phase.

range $0.4 \lesssim g \lesssim 1$. Interestingly, there appears to be an additional phase emerging between the BEC phase and the CSL. Since the system is invariant under the joint operation of time-reversal and reflection, total nearest-neighbor edge current $\mathcal{J}_{nn}^{\text{edge } 1} + \mathcal{J}_{nn}^{\text{edge } 2}$, odd under this joint operation, must vanish for the ground states that respects reflection \times time-reversal symmetry. By performing finite DMRG on finite cylinders, we find that this reflection \times time-reversal symmetry gets spontaneously broken in this parameter regime, and the total nearest-neighbor edge current $\mathcal{J}_{nn}^{\text{edge } 1} + \mathcal{J}_{nn}^{\text{edge } 2}$ attains a finite (positive or negative) value [see Fig. 9(b)]. The profile of the total edge current in Fig. 9(b) clearly indicates twofold degenerate ground-state manifold in this new unknown phase.

We note that the emergence of this additional phase can already be seen in small size clusters, as observed from ED calculations. In Fig. 9(c), we show the fidelity susceptibility as well as the overlap of the exact ground state with various ansatz on the cluster 24a. We find that the additional phase also have a large overlap with ansatz no. 1, where now we optimize the ansatz at each point (orange line). We find that the optimal ansatz in this phase is in the vicinity of the DSL wavefunction. Indeed, the overlap with the DSL wavefunction (blue line), which is obtained by setting the NNN interactions to zero, is remarkably close with the optimal overlap. One possible scenario to explain this observation is that the DSL wavefunction describes the critical wavefunction at the transition from the BEC phase to the unknown phase. A similar scenario was put forward in [54]. Finally, the optimal overlap becomes smaller in the BEC phase, as expected. Instead, in this regime, large overlaps are obtained with the superfluid ansatz, which is defined as the equal-weight superposition of all states at fixed density [62].

IX. CONCLUSIONS

In this paper, we systematically classify CSLs on the honeycomb lattice relevant to Rydberg atom experiments using

the PSG analysis. We show that the CSL wavefunctions constructed from the Gutzwiller-projected parton wavefunctions are able to capture the intermediate disordered phase in chiral Rydberg atom arrays. In particular, our results resolve the previously unclear nature of the intermediate phase found in Ref. [25]. In the context of Rydberg atom experiments, our paper provides a general framework, which can be utilized to search for CSLs in other lattice models. Given the fast experimental progress in the field, it would be interesting to extend our approach to other lattices, which are immediately available in tweezer arrays [2,63].

ACKNOWLEDGMENTS

We thank F. Becca, M. Fleischhauer, and S. Ohler for insightful discussions. M.D. and P.S.T. are grateful to Y. Iqbal for explanations and illuminating clarifications on the parton construction. The work of M.D. and P.S.T. was partly supported by the ERC under Grant No. 758329 (AGEnTh), by the MIUR Programme FARE (MEPH), and by the European Union's Horizon 2020 research and innovation programme under Grant Agreement No. 817482 (Pasquans). P.S.T. acknowledges support from the Simons Foundation through

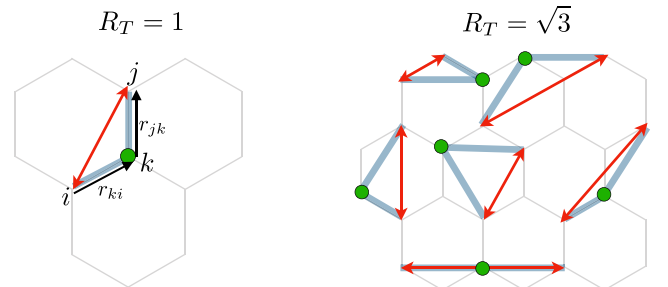


FIG. 10. Schematic representation of the virtual processes generating the density-assisted chiral hopping in the limit $\mu \rightarrow \infty$ when $R_T = 1$ (left) and $R_T = \sqrt{3}$ (right).

Award No. 284558FY19 to the ICTP. G.G. acknowledges support from the European Union's Horizon Europe program under the Marie Skłodowska Curie Action TOPORYD (Grant No. 101106005), from the Deutsche Forschungsgemeinschaft (DFG, German Research Foundation) under Germany's Excellence Strategy –EXC2111 –390814868 and from the ERC Grants No. QSIMCORR, No. ERC-2018-COG, No. 771891. M.D. further acknowledges support from QUANTERA DYNAMITE PCI2022-132919. T.C. acknowledges the support of PL-Grid Infrastructure for providing high-performance computing facility for a part of the numerical simulations reported here.

APPENDIX A: ADIABATIC ELIMINATION AND TRUNCATION OF THE DIPOLAR INTERACTIONS

In the main text we introduced the following Hamiltonian:

$$H_0 = \sum_{i \neq j} \begin{pmatrix} a_i \\ b_i \end{pmatrix}^\dagger \begin{pmatrix} -t_{ij}^a & w_{ij}e^{-i2\phi_{ij}} \\ w_{ij}e^{i2\phi_{ij}} & -t_{ij}^b \end{pmatrix} \begin{pmatrix} a_j \\ b_j \end{pmatrix} + \frac{\mu}{2} \sum_i (n_i^a - n_i^b), \quad (\text{A1})$$

where i labels the sites of a honeycomb lattice, $t_{ij} = t/d_{ij}^3$, $w_{ij} = w/d_{ij}^3$, and d_{ij} is the distance between sites i and j . The hopping phase ϕ_{ij} is the angle between the position vectors of sites i and j . The operators a_i^\dagger and b_i^\dagger create hard-core bosons $[(a_i^\dagger)^2 = (b_i^\dagger)^2 = 0]$ on site i , subject to the constraint $a_i^\dagger b_i^\dagger = 0$ (at most one particle per site).

We argued that when $\mu \gg t_{ij}, w$ one can adiabatically eliminate the a particles, and we considered an effective model where the particle created by a^\dagger is integrated out. Thus, the effective model only includes the hard-core bosonic particle created by b^\dagger , while a particles only appear in virtual processes. When the hopping amplitudes are truncated to nearest-neighbor distance $R_T = 1$ (in units of one lattice spacing) the effective Hamiltonian reads

$$H = - \sum_{\langle ij \rangle} b_j^\dagger b_i - 2g \sum_{\langle\langle ij \rangle\rangle} b_j^\dagger b_i e^{s_{ikj}2\pi i/3} (1 - n_k) + \text{H.c.} + 4g \sum_{\langle ij \rangle} n_i n_j, \quad (\text{A2})$$

where $g = w^2/4t$, the site k is the only possible site between the next-nearest-neighbor sites i and j that can be reached with two virtual nearest-neighbor hoppings, and $s_{ikj} = \text{sign}(r_{jk} \times r_{ki})$ (see Fig 10). The density-density interaction term $n_i n_j$ comes from the virtual process of the form $(b_i a_k^\dagger)(a_j b_i^\dagger) = b_i n_j^\dagger b_i^\dagger$ upon dropping a constant term in the effective Hamiltonian, and its amplitude is *twice* the amplitude of the density-assisted chiral hopping due to the fact that it gets contributions from two virtual processes, starting from sites i and j .

The effective Hamiltonian (2) lives in a reduced Hilbert space and it is thus more amenable to numerical calculations. However, its fairly simple form relies on the truncation of the hopping coefficients t_{ij} and w_{ij} at nearest-neighbor distance. Extending the range of the real hopping R_T up to next-nearest neighbor ($R_T = \sqrt{3}$), leads to six extra chiral hopping terms,

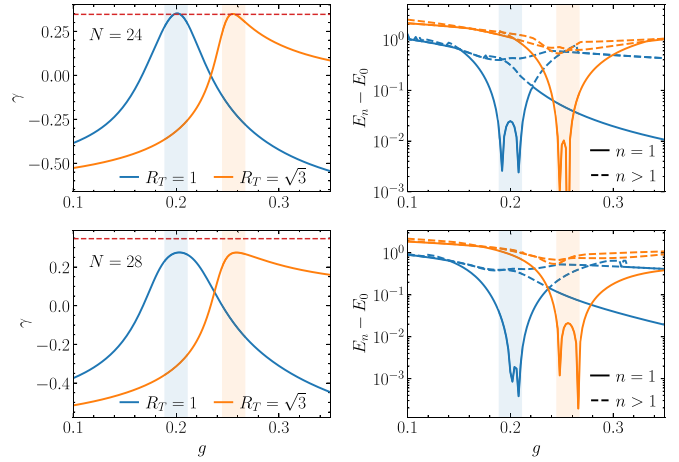


FIG. 11. Ground-state topological entanglement entropy γ (left) and low-lying gaps of the effective Hamiltonian (right) when $\mu \rightarrow \infty$ and for $R_T = a$ (blue) and $R_T = \sqrt{3}a$ (orange), for $N = 24$ (top) and $N = 28$ (bottom). The dashed red horizontal line on the left panels denotes the value $\gamma = \log \sqrt{2}$ expected for a chiral spin liquid ground state.

which are depicted in Fig. 10, as well as an additional density-density interaction term between next-nearest-neighbor sites.

In this Appendix we discuss the effect of finite μ and of larger truncation distances R_T . We do so by performing exact diagonalization for the ground state of the model Eq. (1) both in the limit $\mu \rightarrow \infty$ and at finite μ , when $R_T = 1$ and $R_T = \sqrt{3}$. We refer to “truncated model” in connection to hopping truncation, and to “effective model” in connection to truncation of the Hilbert space following elimination of the a particles. For simplicity we focus on the filling sector where the total number of particles is $N/4$, where N is the number of sites. In fact, the following analysis is aimed at probing the validity of the adiabatic elimination at different hopping truncations R_T , and does not aim at probing the stability of a CSL phase at finite μ and $R_T > 1$ in a generic filling sector.

We now provide numerical evidence from exact diagonalization on periodic clusters of 24 and 28 sites that the $\mu \rightarrow \infty$ effective model hosts a chiral spin liquid phase for both $R_T = 1$ and $R_T = \sqrt{3}$. Figure 11 shows the topological entanglement entropy γ extracted from the partitions depicted in Fig. 4 of the main text, and the lowest eigenvalues of the effective Hamiltonian. Whereas the former exhibits a bump approaching the value $\log \sqrt{2}$, the latter shows an approximate twofold degeneracy of the ground state in the same narrow parameter range, pointing at the emergence of a chiral spin liquid (CSL) regime. We note that the extending R_T from 1 to $\sqrt{3}$ has two effects: it shifts to the right the CSL phase and it changes the nature of the large- g phase, as can be inferred from the different value of γ and structure of the energy levels.

We conclude by studying the effect of finite μ on the ground state of the Hamiltonian (1) with $R_T = \sqrt{3}$. In Fig. (12) we plot the lowest energy gap for several values of μ ranging from 3 to 100. We observe convergence (uniformly in g) to the $\mu = \infty$ curve obtained from the effective model with chiral hopping terms depicted on the right of

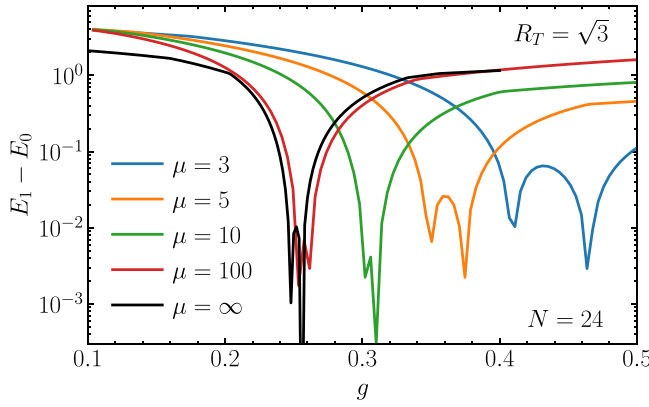


FIG. 12. Lowest energy gap for several values of μ on a periodic cluster with $N = 24$ for the full model Eq. (1).

Fig. 10. Despite the lowest energy gap is not enough to unequivocally identify a CSL phase at finite μ , its functional dependence on g assumes more relevance when compared to the data presented in Fig. 11 and suggests a widening of the CSL regime with decreasing μ (that, we note, is not monotonous).

APPENDIX B: MORE ON PSG CLASSIFICATION

The symmetry group on the honeycomb lattice that we are interested in is generated by translations along x and y , reflection accompanied by time-reversal $T\sigma$, and $\pi/3$ rotation centered on a hexagonal plaquette R . Each algebraic PSG class is characterized by the $SU(2)$ representation of each symmetry generator: $g_x(x, y, s)$, $g_y(x, y, s)$, $g_\sigma(x, y, s)$, $g_R(x, y, s)$, respectively. This can be further simplified by working in a specific gauge. Here, we choose a gauge defined as [45]

$$g_x(x, y, s) = \tau^0, \quad (\text{B1})$$

$$g_y(x, y, s) = \epsilon^x \tau^0, \quad (\text{B2})$$

$$g_\sigma(x, y, s) = \epsilon^{x+y(y+1)/2} g_\sigma(s), \quad (\text{B3})$$

$$g_R(x, y, s) = \epsilon^{xy+x(x-1)/2} g_R(s), \quad (\text{B4})$$

where $\epsilon = \pm 1$, with $\epsilon = -1$ indicates that the unit cell is doubled in the spinon space. Within this gauge choice, each PSG is characterized by the representations of reflection, $g_\sigma(A, B)$, and $\pi/3$ rotation, $g_R(A, B)$, for each sublattice A and B . The representation matrices satisfy the equations (for a detailed derivation, see [45])

$$g_\sigma(A)g_\sigma(B) = g_\sigma(B)g_\sigma(A) = \epsilon_\sigma \tau^0, \quad (\text{B5})$$

$$(g_\sigma(A)g_R(B))^2 = (g_\sigma(B)g_R(A))^2 = \epsilon_{\sigma R} \tau^0, \quad (\text{B6})$$

$$(g_R(A)g_R(B))^3 = (g_R(B)g_R(A))^3 = \epsilon_{RR} \tau^0. \quad (\text{B7})$$

We find 24 different classes of algebraic PSG, which are listed in Table I.

For each algebraic PSG, we now determine the mean-field amplitudes u_{ij} allowed by symmetry up to NNN links. The

TABLE I. PSG representations of point-group symmetries on the honeycomb lattice. Taking into account the two possible signs $\epsilon = \pm 1$ gives 24 distinct algebraic PSG's in total.

No.	$g_\sigma(A/B)$	$g_R(A/B)$	ϵ_σ	$\epsilon_{\epsilon R}$	$\epsilon_{\sigma R}$
1	τ^0/τ^0	τ^0/τ^0	+	+	+
2	$-\tau^0/-\tau^0$	$\tau^0/-\tau^0$	+	-	+
3	$\tau^0/-\tau^0$	τ^0/τ^0	-	+	+
4	$-\tau^0/\tau^0$	$\tau^0/-\tau^0$	-	-	+
5	$-i\tau^2/i\tau^0$	τ^0/τ^0	+	+	-
6	$-i\tau^2/i\tau^0$	$\tau^0/-\tau^0$	+	-	-
7	$i\tau^2/i\tau^0$	τ^0/τ^0	-	+	-
8	$i\tau^2/i\tau^0$	$\tau^0/-\tau^0$	-	-	-
9	$-i\tau^2/i\tau^0$	τ^0/a	+	+	-
10	$-i\tau^2/i\tau^0$	$\tau^0/-a$	+	-	-
11	$i\tau^2/i\tau^0$	τ^0/a	-	+	-
12	$i\tau^2/i\tau^0$	$\tau^0/-a$	-	-	-

consistency conditions for u_1 and u_2 are

$$\begin{aligned} u_1^\dagger &= -(-1)^\chi g_\sigma(A)u_1g_\sigma(B)^\dagger, \\ u_1^\dagger &= g_R(A)g_R(B)g_R(A)u_1g_R(B)^\dagger g_R(A)^\dagger g_R(B)^\dagger, \\ u_2^\dagger &= -(-1)^\chi g_R(B)g_\sigma(A)u_2g_\sigma(B)^\dagger g_R(A)^\dagger, \end{aligned} \quad (\text{B8})$$

where $\chi = 0$ for singlet terms and $\chi = 1$ for triplet terms. The six solutions are shown in the main text. Each u_{ij} can be propagated to the entire lattice using rotations, which act as

$$u_{ij} = g_R(i)u_{R^{-1}(i)R^{-1}(j)}g_R(j)^\dagger, \quad (\text{B9})$$

followed by translations, which act similarly with $g_{x,y}$.

APPENDIX C: OVERLAPS

In Figs. 13(a) and 13(b), we present the overlaps \mathcal{O}_{GW}^{ED} with the low-lying states in the $k = (0, 0)$ momentum sector at $g = 0.1$ and $g = 0.7$. This provides additional insights into

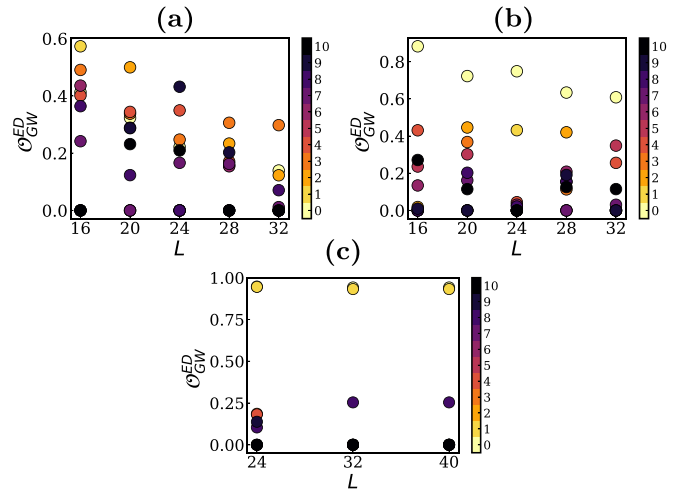


FIG. 13. Overlaps \mathcal{O}_{GW}^{ED} with low-lying states in the $k = (0, 0)$ momentum sector up to the 10th excited state at (a) $g = 0.1$ and (b) $g = 0.7$ for $1/2$ density. (c) Overlaps for $1/4$ density at $g = 0.2$. The markers are colored according to the level of the state.

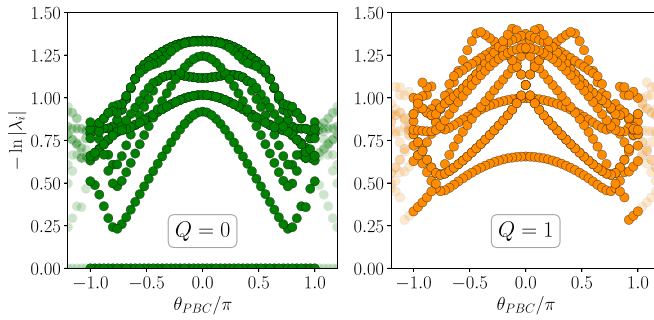


FIG. 14. The spectrum of iMPS transfer matrix in the $Q = 0$ and $Q = 1$ sectors as functions of the twist angle θ_{PBC} for $g = 0.74$ and density $n = 1/2$. Here, we consider an infinite cylinder (geometry I) with periodic width $L_{\text{PBC}} = 4$ and iMPS bond dimension $\chi = 4000$.

the behavior of the overlaps. It can be seen more clearly that at $g = 0.7$, the overlap is the largest with the ground state. Furthermore, there is an additional low-lying state with a modest overlap, possibly representing the topological ground state in the thermodynamic limit. In contrast, such clear pattern is not observed at $g = 0.1$. Instead, the overlaps are seen to be decreasing with system size.

In the case of $1/4$ density, the approximate twofold degeneracy can already be observed clearly from the ED spectra, even on small-size clusters. In addition, as seen in Fig. 13(c), both of the nearly-degenerate states have huge overlaps with the optimal wavefunction ansatz.

APPENDIX D: DETAILS ON DMRG SIMULATIONS

We perform density matrix renormalization group (DMRG) [35–38] simulations using matrix-product state (MPS) [37,38] ansatz for both finite and infinite cylinders, where we take periodic boundary conditions along the one

axis with length $L_{\text{PBC}} = 4$ (8 lattice sites). For finite-size cylinders, we make use of the ITensor library [64] with home-grown DMRG codes. For infinite cylinders, we employ the TeNPy library [65] that uses infinite MPS (iMPS) [66,67] ansatz for infinite DMRG (iDMRG) [68,69] simulations. The MPS bond dimension for the simulations has been taken in the range $\chi \in [2000, 4000]$ resulting in cut-off errors of the order of 10^{-5} to 10^{-7} depending on the system parameters. For completeness, we analyze two different cylinder geometries, namely the geometries I and II as sketched in [70].

APPENDIX E: TRANSFER MATRIX SPECTRUM

The nature of the excitation spectrum can be examined by looking at the spectrum of the transfer matrix of the iMPS ansatz in the iDMRG simulations (see [56,57]). For that purpose, we inject a twist angle θ_{PBC} by putting a θ_{PBC} -flux across the periodic direction cylinder, and follow the spectrum of the iMPS transfer matrix. It is to be noted that the iMPS correlation length ξ_i of a low-energy excitation is related to the transfer matrix eigenvalue λ_i as $\xi_i = -1/\ln|\lambda_i|$.

In Fig. 14, we show the low-lying iMPS transfer matrix spectrum in the charge $Q = 0$ and $Q = 1$ sectors at $g = 0.74$ as a function of the twist angle θ_{PBC} for an infinite cylinder (geometry I). Interestingly, for both $Q = 0$ and 1 , the spectrum is not symmetric around $\theta_{\text{PBC}} = \pi$, which could be attributed to a remnant effect due to the absence of time-reversal symmetry. Nevertheless, the results do not show any signatures of a Dirac cone behavior, which would have appeared as linear dispersion around the minimum gap [56,57]. Instead, the transfer matrix spectrum is consistent with a Chern insulator, where the dispersion becomes quadratic around the minimum gap for $Q = 0$. However, for $Q = 1$, we see a sharp jump in the spectrum around $\theta_{\text{PBC}} \approx 0.9\pi$, which could be a numerical artifact of finite iMPS bond dimension, which we set here to $\chi = 4000$.

- [1] C. Gross and I. Bloch, Quantum simulations with ultracold atoms in optical lattices, *Science* **357**, 995 (2017).
- [2] A. Browaeys and T. Lahaye, Many-body physics with individually controlled Rydberg atoms, *Nat. Phys.* **16**, 132 (2020).
- [3] S. de Léséleuc, V. Lienhard, P. Scholl, D. Barredo, S. Weber, N. Lang, H. P. Büchler, T. Lahaye, and A. Browaeys, Observation of a symmetry-protected topological phase of interacting bosons with Rydberg atoms, *Science* **365**, 775 (2019).
- [4] P. Scholl, M. Schuler, H. J. Williams, A. A. Eberharter, D. Barredo, K.-N. Schymik, V. Lienhard, L.-P. Henry, T. C. Lang, T. Lahaye *et al.*, Quantum simulation of 2D antiferromagnets with hundreds of Rydberg atoms, *Nature (London)* **595**, 233 (2021).
- [5] S. Ebadi, T. T. Wang, H. Levine, A. Keesling, G. Semeghini, A. Omran, D. Bluvstein, R. Samajdar, H. Pichler, W. W. Ho *et al.*, Quantum phases of matter on a 256-atom programmable quantum simulator, *Nature (London)* **595**, 227 (2021).
- [6] G. Semeghini, H. Levine, A. Keesling, S. Ebadi, T. T. Wang, D. Bluvstein, R. Verresen, H. Pichler, M. Kalinowski, R. Samajdar *et al.*, Probing topological spin liquids on a programmable quantum simulator, *Science* **374**, 1242 (2021).
- [7] L. Savary and L. Balents, Quantum spin liquids: A review, *Rep. Prog. Phys.* **80**, 016502 (2016).
- [8] X.-G. Wen, Colloquium: Zoo of quantum-topological phases of matter, *Rev. Mod. Phys.* **89**, 041004 (2017).
- [9] C. Lacroix, P. Mendels, and F. Mila, eds., *Introduction to Frustrated Magnetism* (Springer, Berlin, 2011).
- [10] R. Moessner and J. E. Moore, *Topological Phases of Matter* (Cambridge University Press, Cambridge, 2021).
- [11] M. D. Lukin, M. Fleischhauer, R. Cote, L. M. Duan, D. Jaksch, J. I. Cirac, and P. Zoller, Dipole Blockade and Quantum Information Processing in Mesoscopic Atomic Ensembles, *Phys. Rev. Lett.* **87**, 037901 (2001).
- [12] P. Schauss, Quantum simulation of transverse Ising models with Rydberg atoms, *Quantum Sci. Technol.* **3**, 023001 (2018).
- [13] R. Samajdar, W. W. Ho, H. Pichler, M. D. Lukin, and S. Sachdev, Quantum phases of Rydberg atoms on a kagome lattice, *Proc. Natl. Acad. Sci. USA* **118**, e2015785118 (2021).
- [14] R. Verresen, M. D. Lukin, and A. Vishwanath, Prediction of Toric Code Topological Order from Rydberg Blockade, *Phys. Rev. X* **11**, 031005 (2021).

- [15] G. Giudici, M. D. Lukin, and H. Pichler, Dynamical Preparation of Quantum Spin Liquids in Rydberg Atom Arrays, *Phys. Rev. Lett.* **129**, 090401 (2022).
- [16] G. Giudice, F. M. Surace, H. Pichler, and G. Giudici, Trimer states with \mathbb{Z}_3 topological order in Rydberg atom arrays, *Phys. Rev. B* **106**, 195155 (2022).
- [17] R. Moessner and S. L. Sondhi, Ising models of quantum frustration, *Phys. Rev. B* **63**, 224401 (2001).
- [18] A. W. Glaetzle, M. Dalmonte, R. Nath, I. Rousochatzakis, R. Moessner, and P. Zoller, Quantum Spin-Ice and Dimer Models with Rydberg Atoms, *Phys. Rev. X* **4**, 041037 (2014).
- [19] P. S. Tarabunga, F. M. Surace, R. Andreoni, A. Angelone, and M. Dalmonte, Gauge-Theoretic Origin of Rydberg Quantum Spin Liquids, *Phys. Rev. Lett.* **129**, 195301 (2022).
- [20] R. Samajdar, D. G. Joshi, Y. Teng, and S. Sachdev, Emergent \mathbb{Z}_2 Gauge Theories and Topological Excitations in Rydberg Atom Arrays, *Phys. Rev. Lett.* **130**, 043601 (2023).
- [21] Y. Cheng, C. Li, and H. Zhai, Variational approach to quantum spin liquid in a Rydberg atom simulator, *New J. Phys.* **25**, 033010 (2023).
- [22] D. Peter, N. Y. Yao, N. Lang, S. D. Huber, M. D. Lukin, and H. P. Büchler, Topological bands with a Chern number $C = 2$ by dipolar exchange interactions, *Phys. Rev. A* **91**, 053617 (2015).
- [23] S. Weber, S. de Léséleuc, V. Lienhard, D. Barredo, T. Lahaye, A. Browaeys, and H. P. Büchler, Topologically protected edge states in small Rydberg systems, *Quantum Sci. Technol.* **3**, 044001 (2018).
- [24] S. Weber, R. Bai, N. Makki, J. Mögerle, T. Lahaye, A. Browaeys, M. Daghofer, N. Lang, and H. P. Büchler, Experimentally accessible scheme for a fractional Chern insulator in Rydberg atoms, *PRX Quantum* **3**, 030302 (2022).
- [25] S. Ohler, M. Kiefer-Emmanouilidis, and M. Fleischhauer, Quantum spin liquids of Rydberg excitations in a honeycomb lattice induced by density-dependent Peierls phases, *Phys. Rev. Res.* **5**, 013157 (2023).
- [26] V. Lienhard, P. Scholl, S. Weber, D. Barredo, S. de Léséleuc, R. Bai, N. Lang, M. Fleischhauer, H. P. Büchler, T. Lahaye, and A. Browaeys, Realization of a Density-Dependent Peierls Phase in a Synthetic, Spin-Orbit Coupled Rydberg System, *Phys. Rev. X* **10**, 021031 (2020).
- [27] X.-G. Wen, Quantum orders and symmetric spin liquids, *Phys. Rev. B* **65**, 165113 (2002).
- [28] X.-G. Wen, Quantum order: a quantum entanglement of many particles, *Phys. Lett. A* **300**, 175 (2002).
- [29] S. Bieri, C. Lhuillier, and L. Messio, Projective symmetry group classification of chiral spin liquids, *Phys. Rev. B* **93**, 094437 (2016).
- [30] G. Baskaran and P. W. Anderson, Gauge theory of high-temperature superconductors and strongly correlated Fermi systems, *Phys. Rev. B* **37**, 580 (1988).
- [31] G. Baskaran, Z. Zou, and P. Anderson, The resonating valence bond state and high- T_c superconductivity—A mean field theory, *Solid State Commun.* **63**, 973 (1987).
- [32] In a different context, another example of such occurrence on a Kagome lattice is reported in Ref. [71].
- [33] A. Kitaev and J. Preskill, Topological Entanglement Entropy, *Phys. Rev. Lett.* **96**, 110404 (2006).
- [34] M. Levin and X.-G. Wen, Detecting Topological Order in a Ground State Wave Function, *Phys. Rev. Lett.* **96**, 110405 (2006).
- [35] S. R. White, Density Matrix Formulation For Quantum Renormalization Groups, *Phys. Rev. Lett.* **69**, 2863 (1992).
- [36] S. R. White, Density-matrix algorithms for quantum renormalization groups, *Phys. Rev. B* **48**, 10345 (1993).
- [37] U. Schollwöck, The density-matrix renormalization group in the age of matrix product states, *Ann. Phys.* **326**, 96 (2011).
- [38] R. Orús, A practical introduction to tensor networks: Matrix product states and projected entangled pair states, *Ann. Phys.* **349**, 117 (2014).
- [39] As we report below in Sec. VIII, an extra intermediate phase occurs for $0.25 \lesssim g \lesssim 0.4$.
- [40] T. Dodds, S. Bhattacharjee, and Y. B. Kim, Quantum spin liquids in the absence of spin-rotation symmetry: Application to herbertsmithite, *Phys. Rev. B* **88**, 224413 (2013).
- [41] J. Reuther, S.-P. Lee, and J. Alicea, Classification of spin liquids on the square lattice with strong spin-orbit coupling, *Phys. Rev. B* **90**, 174417 (2014).
- [42] The “singlet” and “triplet” terminology is derived from the discussion of SU(2) spin-rotation symmetric Hamiltonians, which have been extensively studied in the literature. If the state does not spontaneously break the spin-rotation symmetry, only singlet terms are present. However, in the presence of spin-rotation symmetry-breaking perturbations, both terms may be present, and more generally the mean-field Hamiltonian has to be written in terms of a four-component spinor $\Psi = (f_\uparrow f_\downarrow^\dagger f_\downarrow - f_\uparrow^\dagger)^T$. If the spin-rotation is only broken down to U(1), it is still possible to use a two-component spinor representation as in Eq. (3), where the singlet and triplet terms can be present without mixing.
- [43] X.-G. Wen, *Quantum Field Theory of Many-Body Systems* (Oxford University Press, Oxford, 2007).
- [44] X. G. Wen, F. Wilczek, and A. Zee, Chiral spin states and superconductivity, *Phys. Rev. B* **39**, 11413 (1989).
- [45] Y.-M. Lu and Y. Ran, \mathbb{Z}_2 spin liquid and chiral antiferromagnetic phase in the Hubbard model on a honeycomb lattice, *Phys. Rev. B* **84**, 024420 (2011).
- [46] We include all terms that are allowed by symmetry for each link, which in principle can be present in a mean-field state. However, if the mean-field Hamiltonian is restricted in the range of interactions (such as up to NNN interactions in our case), some of the terms can be removed by a gauge transformation.
- [47] M. Hermele, SU(2) gauge theory of the Hubbard model and application to the honeycomb lattice, *Phys. Rev. B* **76**, 035125 (2007).
- [48] Y. Zhang, T. Grover, and A. Vishwanath, Topological entanglement entropy of \mathbb{Z}_2 spin liquids and lattice Laughlin states, *Phys. Rev. B* **84**, 075128 (2011).
- [49] Y. Zhang and A. Vishwanath, Establishing non-Abelian topological order in Gutzwiller-projected Chern insulators via entanglement entropy and modular \mathcal{S} -matrix, *Phys. Rev. B* **87**, 161113(R) (2013).
- [50] R. B. Laughlin, Anomalous Quantum Hall Effect: An Incompressible Quantum Fluid with Fractionally Charged Excitations, *Phys. Rev. Lett.* **50**, 1395 (1983).
- [51] J.-W. Mei and X.-G. Wen, Modular matrices for universal wave-function overlaps in Gutzwiller-projected parton wave functions, *Phys. Rev. B* **91**, 125123 (2015).

- [52] D. Thouless, *Topological Quantum Numbers in Nonrelativistic Physics* (World Scientific, Singapore, 1998).
- [53] A. Wietek, A. Sterdyniak, and A. M. Läuchli, Nature of chiral spin liquids on the kagome lattice, *Phys. Rev. B* **92**, 125122 (2015).
- [54] A. Wietek and A. M. Läuchli, Chiral spin liquid and quantum criticality in extended $S = \frac{1}{2}$ Heisenberg models on the triangular lattice, *Phys. Rev. B* **95**, 035141 (2017).
- [55] Y.-F. Wang, Z.-C. Gu, C.-D. Gong, and D. N. Sheng, Fractional Quantum Hall Effect of Hard-Core Bosons in Topological Flat Bands, *Phys. Rev. Lett.* **107**, 146803 (2011).
- [56] Y.-C. He, M. P. Zaletel, M. Oshikawa, and F. Pollmann, Signatures of Dirac Cones in a DMRG Study of the Kagome Heisenberg Model, *Phys. Rev. X* **7**, 031020 (2017).
- [57] S. Hu, W. Zhu, S. Eggert, and Y.-C. He, Dirac Spin Liquid on the Spin-1/2 Triangular Heisenberg Antiferromagnet, *Phys. Rev. Lett.* **123**, 207203 (2019).
- [58] F. Ferrari, A. Parola, and F. Becca, Gapless spin liquids in disguise, *Phys. Rev. B* **103**, 195140 (2021).
- [59] We, however, note that the finite volume effects prevent a clear interpretation of this data as a striking signature of topological order: such effects are expected given the observed strong finite-size effects in the numerical simulations.
- [60] We consider two different cylinder geometries for our calculations, namely the geometries I and II, as demarcated in [70].
- [61] S.-J. Gu and H.-Q. Lin, Scaling dimension of fidelity susceptibility in quantum phase transitions, *Europhys. Lett.* **87**, 10003 (2009).
- [62] X.-G. Wen, Topological order: from long-range entangled quantum matter to a unified origin of light and electrons, *ISRN Condensed Matter Physics* **2013**, 1 (2013).
- [63] D. Barredo, V. Lienhard, S. de Léséleuc, T. Lahaye, and A. Browaeys, Synthetic three-dimensional atomic structures assembled atom by atom, *Nature (London)* **561**, 79 (2018).
- [64] M. Fishman, S. R. White, and E. M. Stoudenmire, The iTensor software library for tensor network calculations, *SciPost Phys. Codebases*, 4 (2022).
- [65] J. Hauschild and F. Pollmann, Efficient numerical simulations with Tensor Networks: Tensor Network Python (TeNPy), *SciPost Phys. Lect. Notes*, 5 (2018), code available from <https://github.com/tenpy/tenpy>.
- [66] G. Vidal, Classical Simulation of Infinite-Size Quantum Lattice Systems in One Spatial Dimension, *Phys. Rev. Lett.* **98**, 070201 (2007).
- [67] J. A. Kjäll, M. P. Zaletel, R. S. K. Mong, J. H. Bardarson, and F. Pollmann, Phase diagram of the anisotropic spin-2 XXZ model: Infinite-system density matrix renormalization group study, *Phys. Rev. B* **87**, 235106 (2013).
- [68] I. P. McCulloch, Infinite size density matrix renormalization group, revisited, [arXiv:0804.2509](https://arxiv.org/abs/0804.2509).
- [69] G. M. Crosswhite, A. C. Doherty, and G. Vidal, Applying matrix product operators to model systems with long-range interactions, *Phys. Rev. B* **78**, 035116 (2008).
- [70] Y.-C. He, S. Bhattacharjee, R. Moessner, and F. Pollmann, Bosonic Integer Quantum Hall Effect in an Interacting Lattice Model, *Phys. Rev. Lett.* **115**, 116803 (2015).
- [71] W. Zhu, S. S. Gong, and D. N. Sheng, Interaction-driven fractional quantum Hall state of hard-core bosons on kagome lattice at one-third filling, *Phys. Rev. B* **94**, 035129 (2016).
- Correction:* A third affiliation has been added for the second author.